Article

Experiments reveal extreme water generation during planet formation

https://doi.org/10.1038/s41586-025-09816-z

Received: 27 May 2025

Accepted: 27 October 2025

Published online: 30 October 2025

Check for updates

F. Miozzi[1,4]✉, A. Shahar[1], E. D. Young[2], J. Wang[1], A. Steele[1], S. Borensztajn[3], S. M. Vitale[1], E. S. Bullock[1], N. Wehr[3] & J. Badro[3]

The most abundant type of planet discovered in the Galaxy has no analogue in our Solar System and is believed to consist of a rocky interior with an overlying thick H_2-dominated envelope. Models have predicted that the reaction between the atmospheric hydrogen and the underlying magma ocean can lead to the production of notable amounts of water. However, the models suffer from the current lack of experimental data on the reaction between hydrogen and silicate melt at high pressures and temperatures. Here we present new experimental results designed to investigate this interaction. Laser heating diamond anvil cell experiments were conducted between 16 GPa and 60 GPa at temperatures above 4,000 K. We find that copious amounts of hydrogen dissolve into the silicate melt with a large dependence on temperature rather than pressure. We also find that the reduction of iron oxide leads to the production of marked amounts of water along with the formation of iron-enriched blebs. Altogether, the results indicate that the typical processes attending planet formation will result in substantial water production with repercussions for the chemistry and structure of the planetary interior as well as the atmosphere.

Hydrogen, the principal constituent of primary atmospheres, plays a fundamental part in planetary accretion. Its interaction with the planetary interior—particularly the hot magma ocean—establishes the boundary conditions for chemical evolution, thereby influencing the structure, dynamics and marking a crucial stage in the formation of planet[1,2]. Notably, two key reactions are proposed to dominate this stage of accretion. The first involves the reduction of FeO in the melt through reaction with atmospheric H_2, to form Fe and H_2O according to $FeO + H_2 = Fe + H_2O$ (refs. 2,3). The second entails the ingassing of hydrogen into the silicate melt through the equilibrium: $H_2^{gas} = H_2^{melt}$ (for example, refs. 4,5). The extent of change that these reactions can cause on the interior depends mainly on the solubility of hydrogen in the melt and how it changes with pressure and temperature. Constraining solubility is fundamental as the silicate melt can act as a sink for hydrogen, trapping it in the mantle. There, among other reactions, hydrogen can reduce other species to produce water, which can then partition between the silicate melt and the overlying atmosphere. Indigenous formation of water by this reaction has been recognized as a possibility[6,7] but is yet to be established in the laboratory.

Recent modelling studies have investigated the equilibration of a magma ocean with a hydrogen-rich atmosphere, focusing their application to sub-Neptunes, the most abundant type of exoplanet discovered and with no analogue in the Solar System[3,7,8]. Many sub-Neptunes are thought to have molten rocky interiors enveloped by dense H_2 atmospheres. These atmospheres act as a thermal blanket, keeping magma oceans hot for billions of years[9,10] during which interaction between these two reservoirs can lead to water formation[8,11]. The bulk of the experimental work relevant to this system, to date has focused on (1) assessing solubility in evolved melt compositions[4,12], at low pressure and often without iron; (2) the reaction of simplified systems with hydrogen as MgO + Fe (ref. 13) or Fe_2O_3 and $(Mg_xFe_x)O$ (ref. 14); or (3) investigating hydrogen partitioning into the metal core of terrestrial planets[15,16]. Experimental challenges arise from the extremely high temperature required to melt silicates with a primordial composition in the required pressure range, working with hydrogen gas without breaking diamonds or losing the sample and recovering intact samples with sufficient area to perform analytical analyses.

Here we present new experiments investigating the interaction between a hydrogen-bearing atmosphere and a primitive iron-bearing magma ocean at high pressure and high temperature. The silicate was equilibrated with hydrogen gas and heated to above melting temperatures. The experiments were designed to investigate whether there is a combined effect of FeO reduction and H_2 ingassing, as hypothesized in previous studies[17,18], and assess hydrogen solubility in the silicate melt. Our results represent, to our knowledge, the first experimental evidence of hydrogen ingassing and FeO reduction from a primitive mineralogical system from the high-pressure interaction with H_2 and the formation of an Fe-dominated phase. We report a net increase in the hydrogen content of the melt with respect to previous measurements at lower pressure and temperature[12]. Finally, we show evidence of the presence of a free fluid phase in the recovered experiments. Taken together the results provide insights into the processes taking place during atmosphere–magma ocean interaction in the early stages of planetary evolution and in the interior of rocky planets.

[1]Earth and Planets Laboratory, Carnegie Institution for Science, Washington, DC, USA. [2]Department of Earth, Planetary, and Space Sciences, University of California Los Angeles, Los Angeles, CA, USA. [3]Université Paris Cité, Institut de physique du globe de Paris, CNRS, Paris, France. [4]Present address: Department of Earth and Environmental Sciences, University of Pavia, Pavia, Italy. ✉e-mail: fmiozzi@carnegiescience.edu

Chemistry and hydrogen content

Laser-heated diamond anvil cell experiments were performed at pressures between 16 GPa and 60 GPa. Platelets of pyrolytic composition were loaded in an Ar–H_2 mixture, heated at temperatures above 4,000 K (refs. 19,20) (Table 1 and Supplementary Table 1) and recovered and prepared for NanoSIMS analyses with a newly developed protocol (Methods and Supplementary Information).

In the three samples recovered from lower-pressure experiments (that is, Exp_11, Exp_12 and Exp_13), the melt pocket crystallized in concentric layers around a resin-filled cavity. Overall, the silicates show minimal fracturing, limited to the boundaries between layers, and remain well consolidated (for example, Exp_12 in Fig. 1a). The crystallized solids assemblage occupies the outermost layer, whereas the residual melt occupies the innermost layer (Supplementary Text 1 and Supplementary Table 2) and is in contact with the cavity. At the boundary, rounded Fe-enriched blebs are observed (SupplementaryText 2 and Supplementary Figs. 3–5). The cavity has an oblate shape in most samples (Supplementary Fig. 5). The observation of rounded central cavities is new for diamond anvil cell experiments as usually the melt or a metallic phase occupies the central portion of the sample (for example, refs. 21,22). At higher pressure, in Exp_09, the silicates present more fractures. The cavity is flat and elongated (Supplementary Fig. 6). The Fe-enriched blebs are almost dome-shaped and the border with the silicates is irregular with respect to the lower pressure samples (Supplementary Fig. 4). Finally, the highest-pressure sample (Exp_10) shows extremely different characteristics. The silicates present an extensive network of fractures and are poorly consolidated (Supplementary Fig. 6). The cavity is much smaller, and little, irregular and randomly distributed cavities are also visible. The

Table 1 | Experimental conditions and results of NanoSIMS analyses

Sample	Pressure before heating (GPa)	Temperature ± 150 (K)	Measured water (wt%)	Combined uncertainty
Exp_09	46.2	4,500–4,600	5.30	0.10
Exp_10	60	4,700	5.40	0.30
Exp_11	16	4,000	5.60	0.10
Exp_12	22.4	4,100	6.50	0.10
Exp_13	30.7	4,100–4,200	5.90	0.10
Exp_10s (crystallized solids)	60	4,700	0.81	0.01

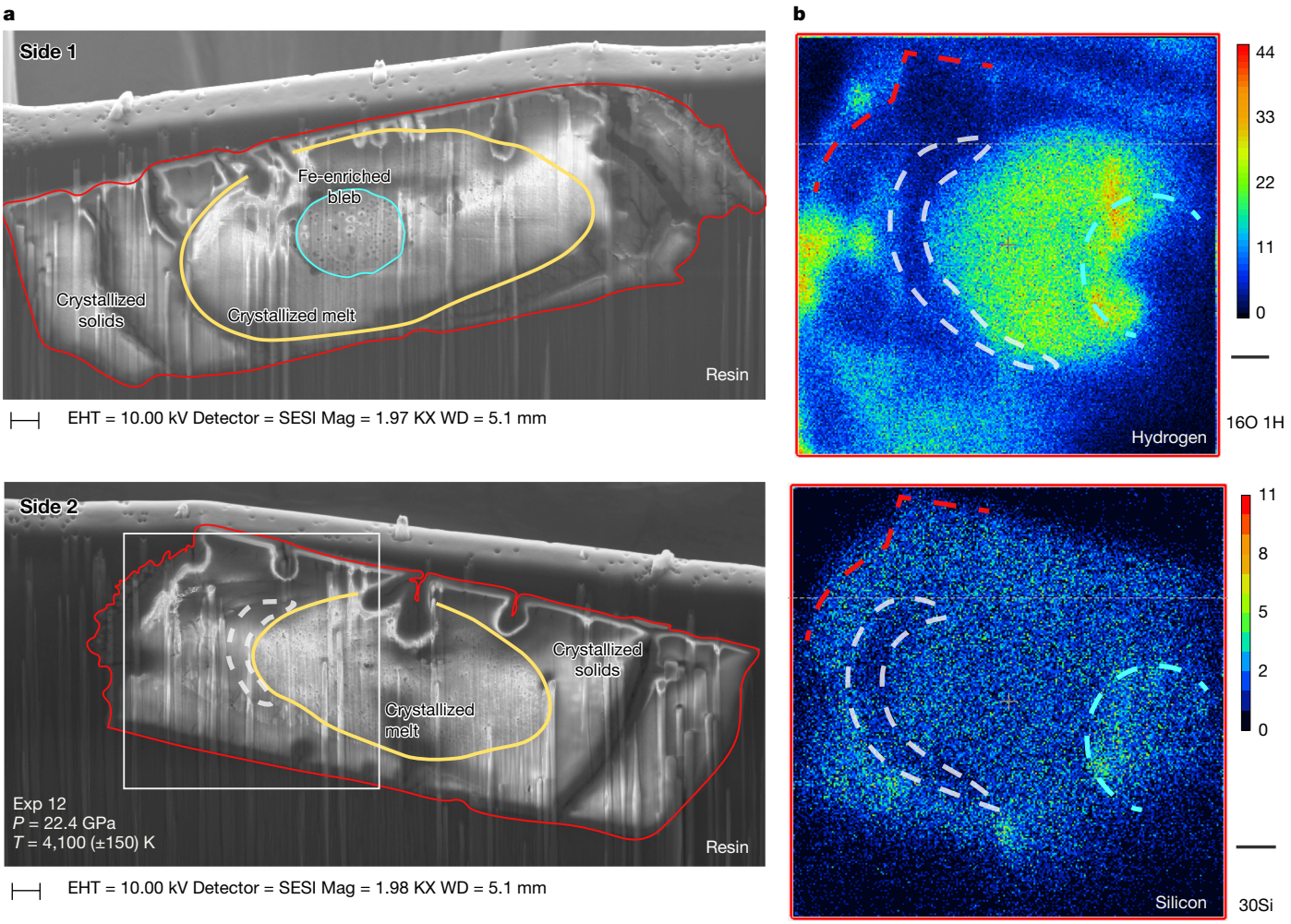

Fig. 1 | Example of images of electrons and ions for one of the samples. **a**, Scanning electron microscope (SEM) images collected on the two sides of the sample during milling with a focused ion beam (FIB). Red lines define the sample. The crystallized melt is characterized by extensive presence of nanometric bubbles. The image of the section of the sample with the visible cavity is in Supplementary Fig. 5. **b**, Maps of hydrogen and silicon collected with the NanoSIMS on a portion of the sample (shown as a white box in the SEM image). Dashed lines serve as a guide for the eye. Red shows the sample boundary, white shows a portion of the crystallized solids and blue shows the portion behind a Fe-enriched bleb. The colour bar represents the intensity of the signal from the corresponding mass for each pixel. In the hydrogen map, the sample shows extremely high counts in the melt. Scale bars, 2 µm (**a**); 3 µm (**b**).

Fe-enriched bleb has an irregular shape and is intertwined with the silicates.

In all of the samples homogeneously distributed nanometric bubbles are visible in the melt. The melt also exhibits a higher Ca content with respect to the crystallized solids (see Supplementary Fig. 2 for an example). Importantly, FeO is absent from the melt in all samples excluding Exp_13 (Supplementary Fig. 3). All the Fe-enriched blebs show some texturing (Supplementary Text 2 and Supplementary Fig. 4).

The hydrogen content was measured with a Cameca NanoSIMS 50L (Table 1 and Fig. 1 and Supplementary Fig. 7). The instrument detects dissolved hydrogen species that are then reported as water (water equivalent), regardless of the speciation that H might have in the sample (that is, H_2, H_2O or OH^-). Accordingly, we provide NanoSIMS results as water and possible alternatives to water equivalent are reported in Supplementary Table 2. In all of the samples, between 5 wt% and 6 wt% water was measured in the quenched silicate melt (Table 1 and Supplementary Fig. 8) and, 1 wt% water was measured in the crystallized solids of sample Exp_10 (Supplementary Fig. 9).

Discussion

The measured water and presence of nanometric bubbles, along with the absence of FeO, and formation of Fe-enriched blebs confirm hydrogen ingassing in the melt and FeO reduction with water production. Accordingly, two processes occur during silicate melt–hydrogen interaction. One is hydrogen incorporation in the melt, as evidenced by the NanoSIMS data, in which the dissolved H_2 can be in the molecular form or as hydroxyl groups. The second is oxide reduction, particularly FeO, and water production, forming a free fluid phase. The latter is heavily supported by the observation of empty cavities in the lower-pressure samples. At the experimental conditions, the water phase would coexist with the melt and the Fe-enriched blebs as separate phases. It would then escape the sample during recovery at ambient conditions, leaving behind an empty cavity. If all the FeO is reduced, about 6 wt% FeO in the starting material would yield about 1.6 wt% water. This represents a lower bound, as other oxides might also reduce and contribute water. NanoSIMS hydrogen measurements similarly reflect a lower solubility limit. The empty bubbles in the silicate melt, probably a product of temperature quench[13], contained exsolved volatiles that were permanently lost on focused ion beam (FIB) milling.

We interpret our observations of Exp_10 (Supplementary Fig. 6) as quench from a single phase, resulting in a less consolidated sample with a widespread network of fractures and irregular boundaries between the different phases. We infer that at these higher conditions the system encountered a solvus (binodal), the boundary above which all phases become miscible and exist as a single phase[23]. This interpretation is consistent with previous observations on simplified systems[13]. In this framework, the P–T conditions for Exp_09 should be close to complete miscibility as it shows features of both the low- and high-pressure samples.

To understand the effects of planetary sizes and conditions on hydrogen solubility into a silicate melt, we parameterize the dependence from pressure and temperature. In the absence of direct evidence of the speciation of hydrogen from our experiments, we model it as H_2 following previous studies[4,12]. We combined our data with the low-pressure solubility data for basaltic melt[12] and considered only H_2 diffusion in the melt, equating the chemical potentials for $H_{2,gas}$ and $H_{2,melt}$ (see Methods for details). Using P and T, $\ln X_{H_2melt}$ from the experiments, multivariate regression over all the experiments results in $\Delta G^{0,*} = 30.577 \pm 6.22$ kJ/mol, $\Delta V = 1.93 \times 10^{-7}$ m^3 mol^{-1} and $f H_2 = 40{,}979$ Pa, the latter corresponding to a mole fraction of the hydrogen in the gas of 1.86×10^{-6}, suggesting the hydrogen in the gas was almost fully dissolved into the sample.

Hydrogen solubility varies with temperature but only weakly with pressure (Fig. 2), showing a slight decrease in the mole fraction of H_2 in the melt with increasing pressure at constant temperature. The solid–melt partitioning coefficient $D_{sil\text{-}melt} = 0.151$ ($\pm$ 0.186) from Exp_10 shows that hydrogen preferentially enters the melt during crystallization.

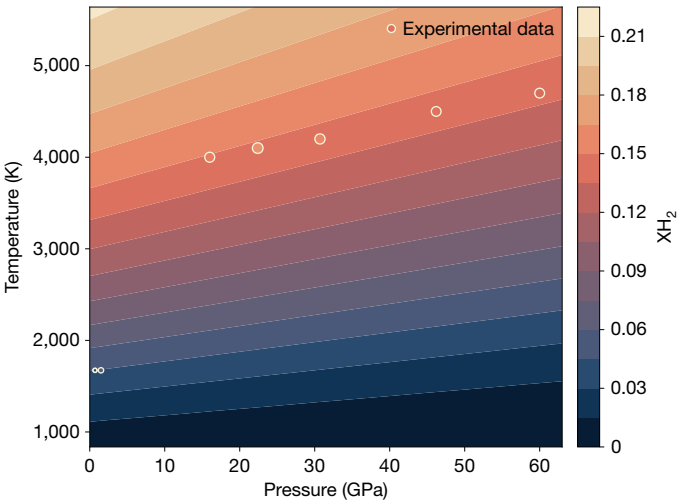

Fig. 2 | Dependency of solubility on pressure and temperature. Coloured contours are the mole fraction of H_2 in the melt recalculated with the parameters fitting the equations. Symbols represent the content measured in the experiments (see also Supplementary Fig. 8). The data below 10 GPa are from ref. 12. The size of the symbols is scaled with hydrogen content.

Implications for planetary interiors

Our results advance our understanding of water production during formation and evolution of planetary bodies and are key to explaining the aspects of the interiors and atmospheres of sub-Neptunes. Previous experimental works focused on a smaller pressure range, investigating only simplified systems in a qualitative manner. By contrast, theoretical work investigated the interaction in the complex system, but key parameters such as the solubility of hydrogen at relevant conditions were still unknown. Here we provide an experimentally derived framework for the interaction of a multi-oxide mineralogical system with hydrogen. We show conclusively that a significant amount of hydrogen is dissolved in the melt, that FeO is reduced to Fe and that the water produced from the reaction forms a free fluid phase at lower pressure and becomes miscible with the silicates above 45 GPa (Fig. 1 and Supplementary Figs. 5 and 6). Moreover, reduction of other oxides present in the melt can represent an additional pathway for water formation[8,17]. Qualitatively our experimental results are aligned with recent literature on exoplanets, predicting a high volume of endogenous water resulting from magma ocean–atmosphere interaction[11,24]. In planetary interiors, the amount of water produced and its fate depend on the available oxides and crucially on the degree of interaction between the silicate melt and the hydrogen. For planetary bodies not massive enough to retain an atmosphere in the early magma ocean stage, hydrogen ingress is probably limited[8]. However, once planets grow to the order of about 0.25 Earth masses or greater[2], H_2-rich envelopes can be retained with magma oceans beneath, leading to the ingassing of substantial amounts of hydrogen and the production of endogenous water. Temperature will control hydrogen solubility, and the dynamic nature of the magma ocean will control oxide delivery to the surficial portions and reduction. It is possible to predict scenarios in which water gets released into the atmosphere creating a steam atmosphere or scenarios in which it is entrained in the magma ocean and accumulates at depth (Fig. 3). Characterizing the dynamic magma ocean and the consequences

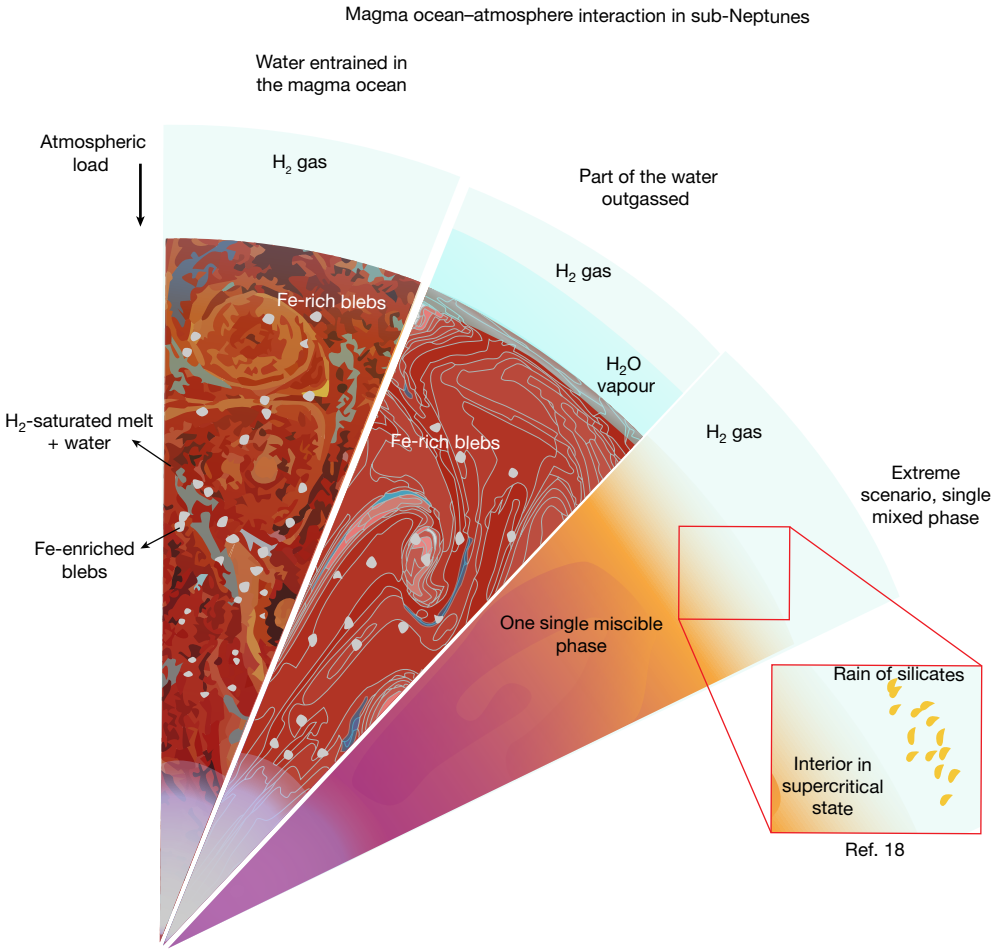

Fig. 3 | Conceptual illustration of three possible scenarios for interior–atmosphere interaction in sub-Neptunes. Left, the free fluid phase and Fe-enriched blebs are entrained in the magma ocean. Centre, water is outgassed to create a steam atmosphere while the Fe-enriched blebs sink toward the centre. Right, extreme scenario in which all phases are miscible.

for the budgets of volatiles is challenging. Nevertheless, our results underscore the importance of such investigations, as hydrogen and water might be significantly more prevalent than previously anticipated for planets accreting with a hydrogen atmosphere overlying molten interiors.

Understanding volatile-rich systems is pivotal for exploring a potential feature of sub-Neptunes: complete miscibility between phases, forming one single mixed phase in the supercritical state in the mantle[18] (Fig. 3). The boundary between a standard interior with separate phases and one in the supercritical state is the position of the solvus for the system in equilibrium with volatiles. Our results indicate complete miscibility, and thus conditions above the pyrolite + H_2 solvus at pressures above 45 GPa and temperatures above 4,500 K for the hydrogen concentration of our experiments. Ab initio calculations performed on the $MgSiO_3$ + H_2 system report full miscibility in a pressure and temperature range consistent with our experiments[25].

Ultimately, along with water production, FeO reduction also implies the formation of an Fe-rich phase. Whether this phase sinks to the core depends on its chemical and physical properties as well as the mass of the planet. For smaller planets, the iron-rich phase is expected to sink to the core (for example, Earth). For more massive planets, in which temperatures are higher, the concentration of light elements in the Fe-rich phase formed through this process may render it so under-dense as to be neutrally buoyant[18].

Notwithstanding the uncertainties regarding complete miscibility, our experimental results indicate an alternative pathway for the incorporation of water into planetary interiors. The hydrogen solubility measured in the quenched silicate melt shows that significant amounts of hydrogen can be stored in a magma ocean while water is being formed concurrently. The storage mechanisms may have unexplored, yet potentially important, effects on the physical and chemical properties of these systems and consequently on the large-scale properties and habitability of a planet.

Online content

Any methods, additional references, Nature Portfolio reporting summaries, source data, extended data, supplementary information, acknowledgements, peer review information; details of author contributions and competing interests; and statements of data and code availability are available at https://doi.org/10.1038/s41586-025-09816-z.

1. Elkins-Tanton, L. T. Magma oceans in the inner Solar System. *Annu. Rev. Earth Planet. Sci.* **40**, 113–139 (2012).
2. Young, E. D., Shahar, A. & Schlichting, H. E. Earth shaped by primordial H_2 atmospheres. *Nature* **616**, 306–311 (2023).
3. Kite, E. S., Fegley, B. Jr., Schaefer, L. & Ford, E. B. Superabundance of exoplanet sub-Neptunes explained by fugacity crisis. *Astrophys. J. Lett.* **887**, L33 (2019).
4. Foustoukos, D. I. Molecular H_2 in silicate melts. *Geochim. Cosmochim. Acta* **389**, 125–135 (2025).
5. Sharp, Z. D. Nebular ingassing as a source of volatiles to the terrestrial planets. *Chem. Geol.* **448**, 137–150 (2017).
6. Ikoma, M. & Genda, H. Constraints on the mass of a habitable planet with water of nebular origin. *Astrophys. J.* **648**, 696–706 (2006).
7. Mizuno, H., Nakazawa, K. & Hayashi, C. Dissolution of the primordial rare gases into the molten Earth's material. *Earth Planet. Sci. Lett.* **50**, 202–210 (1980).

8. Schlichting, H. E. & Young, E. D. Chemical equilibrium between cores, mantles, and atmospheres of super-Earths and sub-Neptunes and implications for their compositions, interiors, and evolution. *Planet. Sci. J.* **3**, 127 (2022).
9. Vazan, A., Ormel, C. W. & Dominik, C. Effect of core cooling on the radius of sub-Neptune planets. *Astron. Astrophys.* **610**, L1 (2018).
10. Ginzburg, S., Schlichting, H. E. & Sari, R. Super-Earth atmospheres: self-consistent gas accretion and retention. *Astrophys. J.* **825**, 29 (2016).
11. Rogers, J. G., Schlichting, H. E. & Young, E. D. Fleeting but not forgotten: the imprint of escaping hydrogen atmospheres on auper-Earth Interiors. *Astrophys. J.* **970**, 47 (2024).
12. Hirschmann, M. M., Withers, A. C., Ardia, P. & Foley, N. T. Solubility of molecular hydrogen in silicate melts and consequences for volatile evolution of terrestrial planets. *Earth Planet. Sci. Lett.* **345–348**, 38–48 (2012).
13. Kim, T. et al. Stability of hydrides in sub-Neptune exoplanets with thick hydrogen-rich atmospheres. *Proc. Natl Acad. Sci. USA* **120**, e2309786120 (2023).
14. Horn, H. W., Prakapenka, V., Chariton, S., Speziale, S. & Shim, S.-H. Reaction between hydrogen and ferrous/ferric oxides at high pressures and high temperatures—implications for sub-Neptunes and super-Earths. *Planet. Sci. J.* **4**, 30 (2023).
15. Clesi, V. et al. Low hydrogen contents in the cores of terrestrial planets. *Sci. Adv.* **4**, e1701876 (2018).
16. Tagawa, S. et al. Experimental evidence for hydrogen incorporation into Earth's core. *Nat. Commun.* **12**, 2588 (2021).
17. Kite, E. S., Fegley, B. Jr., Schaefer, L. & Ford, E. B. Atmosphere origins for exoplanet sub-Neptunes. *Astrophys. J.* **891**, 111 (2020).
18. Young, E. D., Stixrude, L., Rogers, J. G., Schlichting, H. E. & Marcum, S. P. Phase equilibria of sub-Neptunes and super-Earths. *Planet. Sci. J.* **5**, 268 (2024).
19. Pierru, R. et al. Solidus melting of pyrolite and bridgmanite: Implication for the thermochemical state of the Earth's interior. *Earth Planet. Sci. Lett.* **595**, 117770 (2022).
20. Fiquet, G. in *Magmas Under Pressure: Advances in High-Pressure Experiments on Structure and Properties of Melts* (eds Kono, Y. & Sanloup, C.) 115–134 (Elsevier, 2018).
21. Nabiei, F. et al. Investigating magma ocean solidification on Earth through laser-heated diamond anvil cell experiments. *Geophys. Res. Lett.* **48**, e2021GL092446 (2021).
22. Huang, D., Siebert, J. & Badro, J. High pressure partitioning behavior of Mo and W and late sulfur delivery during Earth's core formation. *Geochim. Cosmochim. Acta* **310**, 19–31 (2021).
23. Mibe, K. et al. Second critical endpoint in the peridotite-H_2O system. *J. Geophys. Res.* **112**, 2005JB004125 (2007).
24. Kite, E. S. & Schaefer, L. Water on hot rocky exoplanets. *Astrophys. J. Lett.* **909**, L22 (2021).
25. Stixrude, L. & Gilmore, T. Core-envelope miscibility in sub-Neptunes and super-Earths. Preprint at *Research Square* https://doi.org/10.21203/rs.3.rs-6630955/v1 (2025).

Methods

Diamond anvil cells (DAC) with culet size ranging from 300 μm to 200 μm were used for the experiments. A 200-μm thick rhenium foil was indented to a thickness between 30 μm and 45 μm and drilled with a laser drill system available at the Earth and Planets Laboratory (EPL) of the Carnegie Institution for Science[26]. Samples were produced with a gas-mixing aerodynamic levitation furnace[27] operating at 2,173 K and with an Ar flow (PYR03) or an Ar–H_2 flow (92% Ar and 8% H_2) for PYR05. The mm-sized glass beads were then sliced with a wire saw and double-polished to a thickness of 25–40 μm. Chemical composition was measured with a JEOL JXA-8530F field emission electron microprobe analyser, working with a 15 kV beam and 20 nA current.

The platelets were gently cracked to produce samples with the desired dimensions and were loaded in the experimental chamber along with ruby spheres, used as pressure calibrants. In some cases, small KCl flakes were used to prevent the sample from sticking to the diamond. All the cells were gas-loaded at EPL, with an Ar–H_2 mixture (75% Ar and 25% H_2).

Laser heating experiments were conducted at the Institut de Physique du Globe de Paris (IPGP), France. The samples were heated from both sides using two laser branches that are linearly polarized and where each beam goes through a half-wave plate and a polarizer. The polarizers allowed us to independently change the power reaching each side of the sample, adjusting both sides to have the same temperatures.

Temperature was measured by spectroradiometry on a central 10 μm area. We fit both the Plank and Wien functions, and temperature is constantly monitored from both sides as shown in ref. 20. Samples Exp_09 to Exp_13 were recovered by pouring epoxy resin (EpoTeck 301, from Epoxy Technologies) into the indentation of the gasket while the latter was still mounted on half of the cell. This was pivotal for our study as it allowed us to recover the sample while maintaining its structural integrity. This gives access to a full characterization of the structure and the chemistry of the entire sample, unlike previous studies involving water. After curing, part of the resin was removed with a needle to expose a sufficient portion of the culet at the bottom and cut the metal with the picosecond laser machining system available at IPGP. With this procedure, the recovered samples are like standard DAC-recovered samples (that is, the Re-disk with the sample inside) except for the resin present on top of the experimental chamber. As having to go through resin is not ideal for FIB milling, the samples were mounted upside down on a carbon dot. Samples were gold-coated and milled using the Auriga 40 Zeiss FEG Ga^+ FIB and FEG-SEM, equipped with a Bruker EDX detector at IPGP. The samples were brought to beam coincidence, and trenches were made alternating the two sides until one of the two had a sufficiently big portion of melt without fractures. Quantitative chemical maps (calibrated EDX k-factors; ref. 20) were collected after every cut to monitor the evolution of the chemistry with the milling and identify when the central portion was reached. Before proceeding with the lift-out, Pt was deposited on top of the thick sections and choice were made about where to cut laterally. The samples were too wide (about 90 μm) to be lifted entirely. Finally, sections of 40–60 μm width and 20–40 μm height were lifted and Pt-welded on a Cu-base TEM grid. The stage was then tilted to have the section perpendicular (within 12°) to the SEM column, and elemental maps were collected for 30 min.

To recover the control sample, the cell was slightly opened to release the gasses from the experimental chamber and then placed into a canister with an inflatable membrane. Pressure was increased using ruby fluorescence to track the pressure evolution and the camera to optically monitor changes in the geometry of the experimental chamber. Above 12 GPa, no changes were observed in the geometry of the experimental chamber, but to be sure, the cell was compressed to 25 GPa. The cell was decompressed at a slower rate to avoid cracking the sample.

Before milling, the sample was analysed with a WiTec confocal scanning Raman system (Alpha 300 R) modified for DAC work. Both individual Raman spectra and images were collected on the sample within and outside of the DAC using a 488-nm laser excitation wavelength. Spectra were collected on a Peltier-cooled Andor EMCCD chip, after passing through an *f*/4 300 mm focal length imaging spectrometer, typically using a 600 lines per mm grating. Spectra and maps were background-subtracted, and cosmic ray removed before undergoing principal component analysis all using Witec Project 5 software.

The sample was recovered at EPL by cutting the central portion of the culet using the laser machining instrument. The disc was then mounted on an Si wafer with silver epoxy. At EPL, the sample was milled with an FEI Helios plasma FIB working with Xe^+ following the same procedure as for the other samples milled at IPGP with two exceptions. First, a 10–15 μm tungsten layer was deposited on the entire disc before starting, to protect the front of the cut given the higher currents used with an Xe^+ FIB in respect to a Ga^+ FIB. Second, the higher working current and characteristics of the instrument made it possible to lift the sample with its full width. So instead of cutting trenches to reach the section of interest, the entire width of the disc was ablated. This procedure was not used for the samples milled at IPGP as ablating the rhenium portion of the disk with a Ga^+ FIB is not efficient. For NanoSIMS analyses, the TEM grids with the thick sections were mounted on copper tape with the surface of interest looking upwards. Gas release from the glue component of the tape, in the NanoSIMS vacuum, is considered negligible (Nittler, L., personal communication). As the instrument does not have access to speciation, we used Raman spectroscopy to try to determine the speciation of the hydrogen-bearing species in the melt, but the analyses were not conclusive (Supplementary Text 3).

NanoSIMS analyses

NanoSIMS analyses were performed using a Cs^+ beam with 2 nA current. For each analysed portion, a 15 μm × 15 μm region was pre-sputtered to remove the surface contaminants. The rastered area was then reduced to 10 μm × 10 μm with the area represented by the analyses being a 5 μm × 5 μm portion, because of the beam blanking used to reduce the effect of the edge of the crater. Along with $^{16}OH^-$ and $^{30}Si^-$, specie $^{12}C^-$, $^{19}F^-$, $^{32}S^-$ and $^{35}Cl^-$ were also collected. The timeframe for data collection was 150 s. However, for one of the samples (Exp_09), we needed to cut the analyses at 70 s as a sudden drop in counts signalled that the sample was sputtered away.

We used synthetic forsterite and Suprasil SiO_2 glass to determine background and detection limit, and Alvin 519-4-1, 1833-1, 1846-12, 30-2 and WOK28-3 basaltic glasses for water and other volatiles calibration. The SiO_2 measured in the standards was used to calibrate the acquired species/^{30}Si ratios and define the calibration curve used to determine water content of the samples, given the measured SiO_2 content (see also NanoSIMS data.xlsx). Hydrogen was calculated by dividing the counts obtained for water by a conversion factor calculated dividing two times the molecular weight of hydrogen against the molecular weight of water. Uncertainties reported in Table 1 are the combined uncertainties that includes uncertainties of the collected data determined based on the counting statistics, backgrounds and repeated analyses of 519-4-1 standards, those on the measured SiO_2 content, as well as the one on the calibration curve. Careful consideration of the position of the analytical point was needed, as for most of the samples the Fe-enriched blebs are observed on one side. Similarly, particular attention was given for selecting sections minimizing the number of fractures in the samples. This purpose was achieved in the lower-pressure samples, whereas it was harder for the high-pressure samples because of the lower volume and the important thinning of the sample along the compression axis.

Thermodynamic model

In using the data for basaltic melt from ref. 12, it should be noted that the hydrogen contents at 1 GPa and 3 GPa might be slightly different for pyrolite, as it has less network-forming cations (for example, Ca^{2+} and Al^{2+}) and more network modifiers (for example, Mg^{2+}) than basalt[12,28,29]. However, solubility is suggested to be less affected by composition for small molecular species[30], thus supporting the use of both datasets.

We parametrized the dependence of the solubility from pressure and temperature, considering only the reaction of H_2 diffusion in the melt. Equating the chemical potentials for $H_{2,gas}$ and $H_{2,melt}$ leads to

$$\mu^{0,*}_{H_2melt} + RT\ln X_{H_2melt} + \Delta\overline{V}_{H_2melt} \times \Delta P = \mu^{0,*}_{H_2gas} + RT\ln X_{H_2gas} + RT\ln(P^*/P^{0,*})$$

where asterisk denotes the pure H_2, 0 superscript denotes the standard state (that is, 1 bar, 300 K), $\overline{V}_{H_2melt}$ is the partial molar volume of H_2 in the melt, and we adopt pressure of the pure gas species, P^*, as a surrogate for fugacity of the pure species. Combining the standard-state terms for the pure species into the change in the standard-state molar Gibbs free energy ($\widehat{G}^{0,*}_{H_2gas} - \widehat{G}^{0,*}_{H_2melt}$) and replacing $\ln(\frac{P^*}{P^{0,*}}) + \ln X_{H_2gas}$ with $\ln(\frac{fH_2}{P^{0,*}})$ yields

$$\ln X_{H_2melt} = -\frac{\Delta\widehat{G}^{0,*}}{RT} - \frac{\Delta\overline{V}_{H_2melt}}{RT} \times \Delta P + \ln\frac{fH_2}{P^{0,*}}$$

Using the hydrogen fugacity term to account for both the mole fraction of H_2 in the gas and the non-ideal-gas equation of state for the gas phase avoids assumptions about non-ideal behaviour. We use this expression to derive typical values for the fugacities of hydrogen for the experiments as a group. This is justified by very low values obtained relative to experimental pressures, even when including H_2 fugacity coefficients that range from about 10^2 to 10^4 over our experimental conditions[31]. The R^2 for the fit is 0.91 based on experimental uncertainties. Comparison between the observed and modelled data is in Supplementary Fig. 10. The covariance matrix of the fit was used to calculate the 1σ errors reported for each parameter. The partial molar volume is smaller than the one reported in ref. 12 at 4 GPa and 3,500 K (1.6×10^{-5} m^3 mol^{-1} and 7.3×10^{-6} m^3 mol^{-1}, respectively).

Data availability

Source data and the data shown in the figures are provided with this paper.

26. Hrubiak, R., Sinogeikin, S., Rod, E. & Shen, G. The laser micro-machining system for diamond anvil cell experiments and general precision machining applications at the High Pressure Collaborative Access Team. *Rev. Sci. Instrum.* **86**, 072202 (2015).
27. Badro, J. et al. Experimental investigation of elemental and isotopic evaporation processes by laser heating in an aerodynamic levitation furnace. *Comptes Rendus. Géoscience* **353**, 101–114 (2021).
28. Mysen, B. Water-melt interaction in hydrous magmatic systems at high temperature and pressure. *Prog. Earth Planet. Sci.* **1**, 4 (2014).
29. Stolper, E. The speciation of water in silicate melts. *Geochim. Cosmochim. Acta* **46**, 2609–2620 (1982).
30. Gaillard, F., Schmidt, B., Mackwell, S. & McCammon, C. Rate of hydrogen–iron redox exchange in silicate melts and glasses. *Geochim. Cosmochim. Acta* **67**, 2427–2441 (2003).
31. Chabrier, G., Mazevet, S. & Soubiran, F. A new equation of state for dense hydrogen–helium mixtures. *Astophys. J.* **872**, 51 (2019).

Acknowledgements We thank the editor, Linda Elkins-Tanton and two anonymous reviewers for their constructive feedback. F.M. thanks T. Gooding for the discussions about epoxy resin and sample recovery procedures and G. Cascioli, E. Codillo, V. Dobrosavljevic, Z. Geballe and G. Criniti for the support and discussions. This AEThER publication is funded by the Carnegie Institution for Science and the Alfred P. Sloan Foundation under grants G202114194 and G-2025-25284. J.B. acknowledge funding from the European Research Council (ERC) under the Horizon 2020 research and innovation programme of the European Union (grant agreement no. 101019965—ERC advanced grant SEPtiM). This study was supported by LabEx UnivEarthS (ANR-10-LABX-0023) and Idex Université Paris Cité (ANR-18-IDEX-0001) and by the IPGP multidisciplinary programme PARI and Paris–IdF region SESAME grant no. 12015908. E.D.Y. acknowledges funding from NASA grant 80NSSC24K0544.

Author contributions F.M. designed the research, performed the experiments and analyses, analysed the data and drafted the manuscript. A.S. conceived the research, contributed to data analysis and revised the manuscript. J.B. contributed to the experiments, data analysis and revised the manuscript. E.D.Y. contributed to data analysis and revised the manuscript. A.S. contributed to the Raman analyses and edited the manuscript. J.W. performed the NanoSIMS analyses and edited the manuscript. S.B. operated the FIB at IPGP. S.M.V. operated the FIB at EPL. E.S.B. operated the EMPA at EPL. N.W. contributed to the experiments at IPGP.

Competing interests The authors declare no competing interests.

Additional information

Supplementary information The online version contains supplementary material available at https://doi.org/10.1038/s41586-025-09816-z.

Correspondence and requests for materials should be addressed to F. Miozzi.

Peer review information *Nature* thanks Linda Elkins-Tanton and the other, anonymous, reviewer(s) for their contribution to the peer review of this work. Peer reviewer reports are available.